



van Dijk, J. A., Fracasso, A., Petridou, N. and Dumoulin, S. O. (2021) Laminar processing of numerosity supports a canonical cortical microcircuit in human parietal cortex. *Current Biology*, 31(20), 4635-4640.e4.

(doi: [10.1016/j.cub.2021.07.082](https://doi.org/10.1016/j.cub.2021.07.082))

This is the Author Accepted Manuscript.

There may be differences between this version and the published version. You are advised to consult the publisher's version if you wish to cite from it.

<http://eprints.gla.ac.uk/250910/>

Deposited on: 24 March 2022

# 1 Laminar processing of numerosity 2 supports a canonical cortical microcircuit 3 in human parietal cortex

4 Jelle A. van Dijk<sup>1,2,\*</sup>, Alessio Fracasso<sup>1,3,4</sup>, Natalia Petridou<sup>4</sup>, Serge O. Dumoulin<sup>1,2,5,6</sup>

5 <sup>1</sup> Spinoza Centre for Neuroimaging, Amsterdam, NL; <sup>2</sup> Experimental Psychology, Utrecht University,  
6 Utrecht, NL; <sup>3</sup> Institute of Neuroscience and Psychology, University of Glasgow, Glasgow G12 8QB, UK;

7 <sup>4</sup> Radiology Department, Imaging Division, Center for Image Sciences, University Medical Center  
8 Utrecht, NL; <sup>5</sup> Experimental and Applied Psychology, VU University, Amsterdam, NL; Netherlands  
9 Institute for Neuroscience, Royal Netherlands Academy of Sciences, Amsterdam, NL.

10 \*Corresponding author: Jelle A. van Dijk, j.van.dijk@spinozacentre.nl

## 11 Summary

12 As neural signals travel through the visual hierarchy, spatial precision decreases and specificity for  
13 stimulus features increases<sup>1-4</sup>. A similar hierarchy has been found for laminar processing in V1, where  
14 information from the thalamus predominantly targets the central layers, while spatial precision  
15 decreases and feature specificity increases towards superficial and deeper layers<sup>5,6,15-17,7-14</sup>. This  
16 laminar processing scheme is proposed to represent a canonical cortical microcircuit that is similar  
17 across the cortex<sup>11,18-21</sup>. Here, we go beyond early visual cortex and investigate whether processing of  
18 numerosity (the set size of a group of items) across cortical depth in the parietal association cortex  
19 follows this hypothesis. Numerosity processing is implicated in many tasks such as multiple object  
20 tracking<sup>22</sup>, mathematics<sup>23-25</sup>, decision making<sup>26</sup>, and dividing attention<sup>27</sup>. Neurons in the parietal  
21 association cortex are tuned to numerosity, with both a preferred numerosity tuning and tuning width  
22 (specificity)<sup>28-30</sup>. We quantified preferred numerosity responses across cortical depth in the parietal  
23 association cortex with ultra-high field fMRI and population receptive field-based numerosity  
24 modelling<sup>1,28,31</sup>. We find that numerosity responses sharpen, i.e. become increasingly specific, moving  
25 away from the central layers. This suggests that the laminar processing scheme for numerosity  
26 processing in the parietal cortex is similar to primary visual cortex, providing support for the canonical  
27 cortical microcircuit hypothesis beyond primary visual cortex.

## 28 Keywords

29 visual processing; numerosity; cortical organization; fMRI; population receptive fields; computational  
30 modelling

## 31 Results and Discussion

32 We use ultra-high field functional magnetic resonance imaging (fMRI) to investigate whether  
33 processing of numerosity across cortical depth in parietal cortex fits the canonical cortical microcircuit  
34 hypothesis. Ultra-high field MRI allows us to measure both anatomical and functional cortical depth-  
35 dependent signals that reflect information processing across cortical depth (for reviews see<sup>12-  
36 14,17,32,33</sup>).

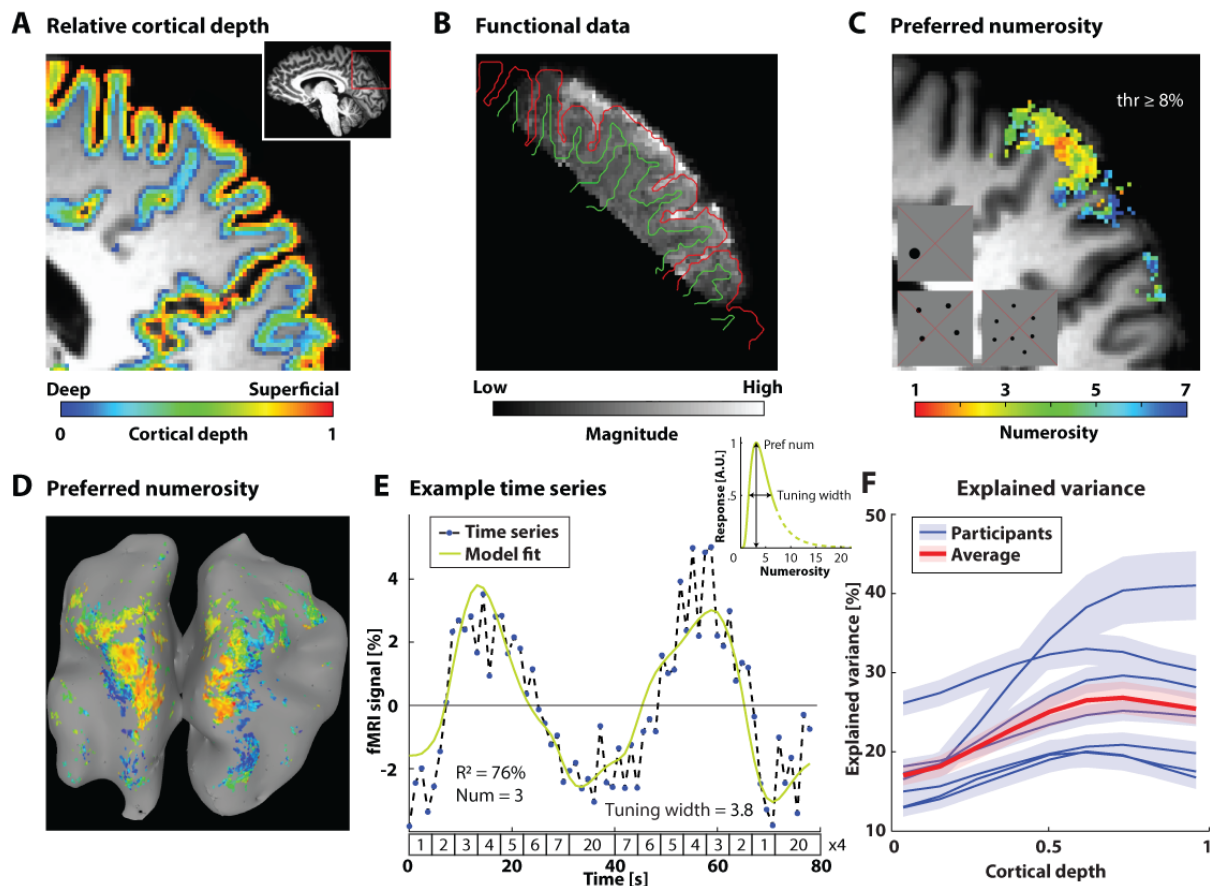
37 Studies using fMRI have revealed a network of cortical areas that are involved in numerosity  
38 processing<sup>27,29,34-38</sup>. Recent fMRI studies have shown that a number of cortical locations involved in

39 numerosity processing are topographically organized, with numerosity preference gradually changing  
40 along the cortical surface<sup>28,31,39</sup>. Neuronal populations in these topographic regions show numerosity  
41 tuning, with large responses for stimuli of a specific numerosity and increasingly smaller responses  
42 when the numerosity of a stimulus is further from the preferred numerosity of that population. A  
43 cluster of numerosity topographic maps involved in numerosity processing is located in the parietal  
44 association cortex.

45 Participants (N=7) viewed stimuli consisting of groups of circles that systematically increased and  
46 decreased in numerosity over time<sup>28</sup> (see inset in Figure 1C, E). Meanwhile, we collected functional  
47 MRI data (0.93 mm isotropic resolution, Figure 1B). We segmented grey matter and obtained a  
48 continuous measure of cortical depth, normalized with respect to cortical thickness<sup>40</sup> (range= 0-1,  
49 <https://nighres.readthedocs.io/en/latest/>, with 0 representing the white matter boundary and 1 the  
50 gray matter/cerebrospinal fluid boundary; Figure 1A). This equi-volume model provides a coordinate  
51 system of cortical depth which is independent from local cortical folding. We sampled across 9 cortical  
52 depth bins, deriving single profiles (see Methods).

53 It is important to note that an acquisition resolution of 0.93 mm isotropic would at best allow to  
54 measure 4 different compartments, assuming a 3-4 mm cortical thickness<sup>41</sup>. However, we obtain 9  
55 separate estimates along normalized cortical depth. We can obtain these estimates thanks to the  
56 folded nature of cortical surface. When measuring MRI signal along cortical depth, we are using a  
57 regular grid (the field-of-view of the acquisition resolution, 0.93 mm isotropic), while we sample signal  
58 from an irregular (folded) portion of the cortex. Thus, the center of a voxel on the regular grid could  
59 be located close to the cerebrospinal fluid surface, close to the white matter surface or anywhere  
60 between the two, thus allowing a denser sampling rate along cortical depth (see Methods).

61 Next, we modeled the numerosity responses<sup>28</sup>, resulting in a preferred numerosity and tuning width  
62 estimate (specificity) for each cortical location, cortical depth, and participant (Figure 1C-E). We  
63 selected all profiles within the field of view of the functional data for which model fits across all depths  
64 exceeded an individual cross-validated explained variance threshold for further analysis. These  
65 individual thresholds were set to the 99<sup>th</sup> percentile of the cross-validated model explained variance  
66 in white matter for each participant ( $M = 8\%$ ,  $SD = 2\%$ , range = 5-12%). Cross-validated model  
67 explained variance generally increased towards the cortical surface (Figure 1F, see Figure S2A for BOLD  
68 amplitude across depth, which follows the same pattern).

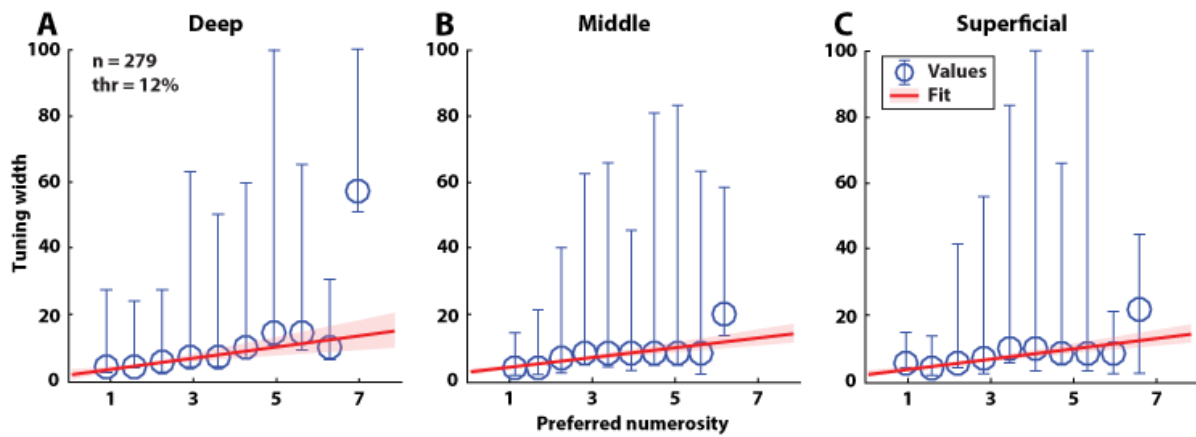


69

70 *Figure 1: Processing steps and model fits. A) Volume-preserving cortical depth map on a partial,*  
 71 *sagittal anatomical slice. Inset: whole brain anatomical slice with the location of the partial slice (red*  
 72 *box). B) Mean susceptibility distortion-corrected functional data registered to the anatomy, with gray*  
 73 *matter-CSF (red) and gray-white matter (green) borders. C) Preferred numerosity results at all depths.*  
 74 *Threshold: cross-validated model  $R^2 = 8\%$ . Insets: Cut-outs of the central portion of example stimulus*  
 75 *displays with numerosity 1, 4, and 7. Stimuli all fell within a 0.75-degree visual angle radius from the*  
 76 *center of fixation. D) Preferred numerosity at the middle depth bin projected on a partial mesh*  
 77 *corresponding to the coverage in A-C), coronal view. Threshold: model  $R^2 = 8\%$ . E) Time-series of an*  
 78 *example voxel (dashed line with blue discrete timepoints) overlaid with best fitting predicted fMRI*  
 79 *response (solid green line). Goodness of fit (model  $R^2$ ) = 76%, preferred numerosity = 3, tuning width =*  
 80 *3.8. Inset top right: Tuning model for the example voxel. Inset below x-axis: stimulus sequence.*  
 81 *Additional examples can be found in Figure S4. F) Model cross-validated explained variance generally*  
 82 *increases towards the cortical surface (cortical surface = 1). Blue shaded regions denote the standard*  
 83 *error of the mean for separate participants. Red shaded region denotes the standard error of the mean*  
 84 *across participants.*

85 Tuning width increases with preferred numerosity

86 For every cortical depth bin, we performed a linear fit on the median tuning width across preferred  
 87 numerosity. The tuning width increased systematically with preferred numerosity across participants:  
 88  $M_{slope} = 1.40$ ,  $SD_{slope} = 0.98$ ,  $Range_{slope} = 0.07 - 4.18$  (see Figure 2 for three example cortical depth bins  
 89 for a participant, and Figure S2C, D for the average fit slope and intercept values across cortical depth  
 90 for each participant).

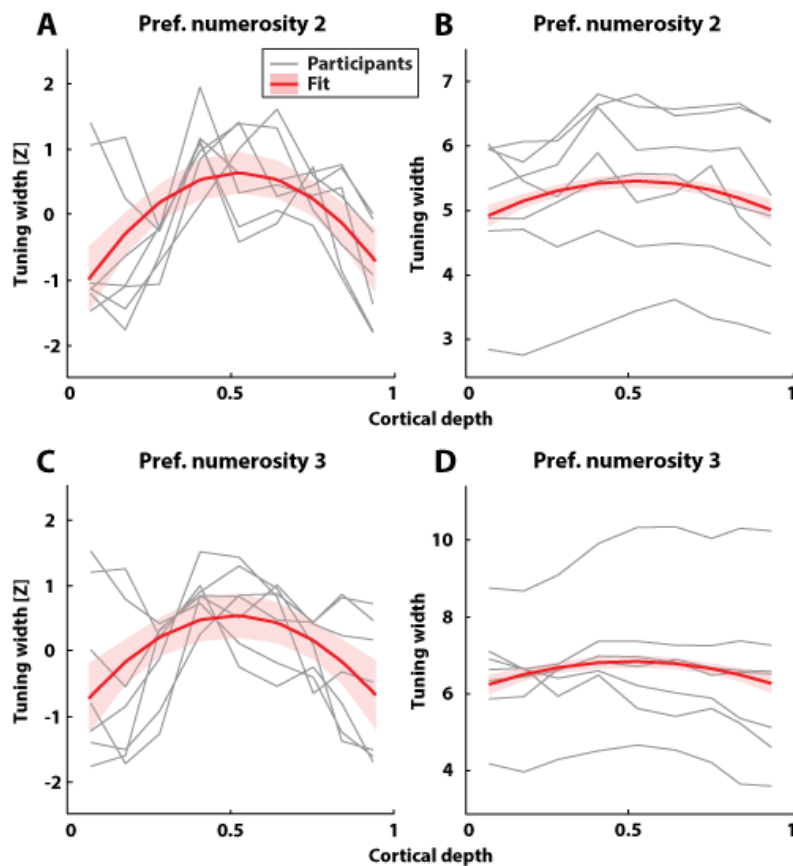


91

92 *Figure 2: Preferred numerosity and tuning width for three example cortical depths for an example*  
 93 *participant. The cross-validated model explained variance threshold (thr) for each sampled depth was*  
 94 *12%. Each panel shows the preferred numerosity versus tuning width. Average normalized depth: 0.18*  
 95 *(deep/infragranular, A), 0.52 (approx. middle/granular, B), and 0.83 (superficial/supragranular, C).*  
 96 *Blue circles and lines represent median preferred tuning width and 95% confidence intervals. Red lines*  
 97 *and shaded regions represent the least-squares median fits and their 95% confidence intervals. Tuning*  
 98 *width consistently increased with increasing numerosity for each cortical depth.*

99 Response specificity sharpens towards deeper and superficial layers

100 To quantify the change in response specificity across cortical depth, we sampled tuning width  
 101 estimates at numerosity 2 and 3. These numerosities were selected as they were most prevalent in  
 102 the data (12 and 9% respectively, see Figure S2B), hence resulting in the most stable estimates. To  
 103 reduce inter-participant variability, the sampled tuning width estimates for each participant were z-  
 104 scored. For both numerosities, the tuning width profiles showed an inverted U-shape across cortical  
 105 depth, with tuning width being largest around the middle cortical depth and decreased both towards  
 106 the deep and superficial cortical depth portions (Figure 3). T-tests on the parameters of individual  
 107 second-degree polynomial fits on the Z-scored tuning width profiles revealed that the inverted U-  
 108 shape of the tuning curve was significant for both sampled numerosities, with parameter values for  
 109 preferred numerosity 2 (Figure 3A, B) of: slope = 8.1, quadratic component = -7.73;  $t(6)_{slope} = 4.01$ ,  $p =$   
 110  $0.007$ ,  $t(6)_{quadratic} = -5.52$ ,  $p = 0.002$ . For preferred numerosity 3 (Figure 3C, D), these values were: slope  
 111 = 6.58, quadratic component = -6.48;  $t(6)_{slope} = 3.05$ ,  $p = 0.022$ ,  $t(6)_{quadratic} = -4.03$ ,  $p = 0.007$ . Fitting  
 112 only a straight line, forgoing the quadratic component, resulted in non-significant results for all model  
 113 parameters and numerosities. The results were highly similar using restrictions in maximum tuning  
 114 width, removing the outer depth bins, using different thresholds (Figure S1), and using the median  
 115 tuning width, rather than sampling at a specific numerosity (Figure S3C). Preferred numerosity does  
 116 not vary significantly across cortical depth (Figure S3A,B).



117

118 *Figure 3: Tuning width profiles show response sharpening with increased processing toward deep*  
 119 *(cortical depth < 0.5) and superficial (cortical depth > 0.5) cortical depth portions. A, C) Z-scored tuning*  
 120 *width, sampled at preferred numerosity 2 and 3 from the median fits for each depth bin (red lines in*  
 121 *Figure 2). Shaded regions represent the 95% between-participant confidence interval of the fit. B, D)*  
 122 *Tuning width, sampled at preferred numerosity 2 and 3. Polynomial fit (red line) and confidence*  
 123 *interval (shaded region) transformed from Z-scored data (A). For all panels: gray lines represent*  
 124 *individual participants. Red lines represent the best second-degree polynomial fit.*

125 Laminar processing of numerosity supports a canonical cortical microcircuit in parietal  
 126 cortex

127 We tested whether the cortical microcircuit hypothesis holds for numerosity processing in human  
 128 parietal cortex. This hypothesis states that cortical information processing follows universal principles  
 129 that are shared across the cortex<sup>18,20,21,42</sup>. To assess the feasibility for this hypothesis for numerosity  
 130 processing in the parietal cortex, we evaluated response specificity (tuning width) profiles across  
 131 cortical depth, elicited by viewing numerosity stimuli. We find that tuning width increases with  
 132 preferred numerosity at individual cortical depths. This increase is consistent with previous findings  
 133 across preferred numerosity at lower resolutions<sup>28,31</sup>. Moreover, we show that specificity for  
 134 numerosity increases towards both superficial and deeper cortical depth portions, as tuning width is  
 135 largest in the central portion and sharpens in the direction of both the superficial and deeper portions  
 136 of cortical depth. This processing hierarchy is similar to that of primary visual cortex<sup>16</sup>. Therefore, we  
 137 suggest that our results provide evidence that the laminar processing hierarchy is preserved across  
 138 the parietal cortex, thus supporting the hypothesis that the increased specificity for stimulus  
 139 dimensions along the laminar hierarchy may represent a canonical cortical microcircuit that may be  
 140 similar across the cortex<sup>11,18–21</sup>.

141 The infra- and supragranular layers receive feedback from regions higher in the hierarchy<sup>6</sup>. Thus, this  
142 feedback also likely contributes to the neural tuning across cortical depth. Therefore, the response  
143 sharpening we observe across cortical depth may be an effect of a combination of feedback  
144 connections from regions higher in the numerosity processing hierarchy, and local processing.

145 Potential vasculature confounds

146 Cortical vasculature varies systematically across cortical depth<sup>43</sup>. Could the tuning width profile thus  
147 be driven by the vasculature rather than neural effects? We think that this is unlikely. First, due to the  
148 local vasculature, signal amplitudes increase monotonically towards the cortical surface<sup>44,45</sup>.  
149 Particularly, vessel diameters -to which gradient echo BOLD is particularly sensitive to- increase  
150 towards the surface, resulting in a steady increase in signal amplitude in that direction<sup>44,46-49</sup>.  
151 Additionally, we assert that larger signal amplitudes are related to increased variance explained  
152 (although the physiological noise levels do scale with signal amplitude<sup>50-52</sup>). Therefore, if the results  
153 were purely driven by the vasculature, we would expect tuning width to show a monotonous decrease  
154 or increase towards the cortical surface. Second, previous work using fMRI across cortical depth in  
155 early visual cortex<sup>15</sup> has shown that the pattern of spatial pooling of visual responses is not a direct  
156 reflection of the cortical vascular organization, and closely resembles neurophysiological  
157 measurements in primates<sup>17</sup>. All in all, it is unlikely that the presented results are merely an artefact  
158 of the inherent properties of the fMRI signal, and we believe that these results reflect signals of neural  
159 origin.

160 In conclusion, we provide evidence that laminar processing for numerosity in the parietal association  
161 cortex follows the same pattern as laminar processing in early visual cortex, with response specificity  
162 increasing away from the central portion of cortical depth both towards the deeper and more  
163 superficial depths. This processing parallels the increasing feature specificity across the visual  
164 processing hierarchy. Thus, we suggest that this finding expands support for the canonical microcircuit  
165 hypothesis stating that laminar processing is organized similarly across the cortex.

166 STAR Methods

## 167 RESOURCE AVAILABILITY

### 168 *Lead contact*

169 Further information and requests should be directed to and will be fulfilled by the lead contact, Jelle  
170 A. van Dijk (j.van.dijk@spinozacentre.nl)

### 171 *Materials availability*

172 This study did not generate reagents.

### 173 *Data and code availability*

174 Data reported in this paper will be shared by the lead contact upon request.

175 All original code has been deposited at XXX and is publicly available as of the date of publication. DOIs  
176 are listed in the key resources table.

177 Any additional information required to reanalyze the data reported in this paper is available from the  
178 lead contact upon request.

## 179 EXPERIMENTAL MODEL AND SUBJECT DETAILS

180 Eight participants (1 female, mean age: 31.4 years, age range 22-45 years old) participated in this  
181 study. All participants were familiar with the MRI environment and had participated in previous  
182 experiments. They had normal or corrected-to-normal visual acuity. All participants signed informed  
183 consent. All experimental procedures were approved by the medical ethics committee of the  
184 University Medical Center Utrecht and adhered to the guidelines of the Declaration of Helsinki. One  
185 participant was excluded due to excessive motion between runs.

## 186 METHODS DETAILS

### 187 *Stimuli*

188 Stimuli were presented on a 32-inch LCD screen, specifically designed for use in an MRI environment<sup>53</sup>.  
189 The screen resolution was 1920 x 1080 pixels, with a screen size of 69.8 x 39.3 cm, a refresh rate of  
190 120 Hz, and a built-in linear luminance look-up table. The display was positioned at the far end of the  
191 bore and was viewed via a mirror positioned in the head coil of the MRI scanner. The total viewing  
192 distance was 220 cm. The total visible vertical extent of the screen subtended 10.2 degrees visual  
193 angle (deg).

194 All stimuli were generated in MATLAB (Mathworks; 2018a) using the Psychophysics toolbox<sup>54,55</sup>. A  
195 large cross consisting of two thin (1 pixel) red diagonal lines starting at the corners of a 10.2 x 10.2  
196 degree invisible square and intersecting in the center of the screen was presented at all times, with a  
197 mean luminance gray background that covered the entire screen. Stimuli consisted of groups of  
198 circles, randomly distributed to be presented entirely within an invisible circle with a 0.75-degree  
199 radius around the center of the screen to minimize eye movements. Each group of circles contained 1  
200 to 7 or 20 circles, with 20 functioning as a baseline. Numerosity 20 was chosen to this end as it is  
201 expected to be well outside the response range of neuronal populations responding to numerosities  
202 1 to 7, while neuronal populations responding to contrast energy would be expected to respond most  
203 strongly to this energy-rich condition<sup>56</sup>. The total surface area (702 pixels) of each group of circles was  
204 constant between different numerosities. This resulted in a decreased size per circle with increasing  
205 numerosity (see inset Figure 1C). A previous study controlled for dot size, crowding, total  
206 circumference, shape, and total area of the numerosity stimuli. The authors observed that there is  
207 little difference between estimates resulting from different stimuli<sup>28</sup>. In the current study we adopted  
208 a constant total area as it equates global stimulus energy (contrast) among different numerosities. On  
209 regular trials, the circles were black. However, groups of white circles with the same numerosity were  
210 randomly presented instead of black ones on approximately 9% of the trials. Participants were asked  
211 to respond to these presentations by means of a button press and foveate the middle of the fixation  
212 cross during the entire experiment. No numerosity-related judgments were required. Average task  
213 performance was 97.4 % correct (range 69.8 - 100 % for individual runs).

214 Stimuli were presented for 350 ms, followed by 250 ms of mean luminance gray. Numerosities 1 to 7  
215 were displayed sequentially, first in ascending order and then in descending order. Each numerosity  
216 was presented six times (3600 ms including mean luminance gray presentations) before the next  
217 numerosity was presented. Numerosity 20 was presented after each ascending or descending sweep.  
218 These presentations of numerosity 20 lasted 14400 ms (24 presentations). The combination of the  
219 ascending and descending sweep interleaved with numerosity 20 was repeated 4 times for each run.  
220 Each run started with 20 presentations of numerosity 20 (12000 ms). The total presentation time for  
221 one run was 5 m 28.8 s. The stimulus sequence and displays were near-identical to those previously  
222 used by Harvey and colleagues<sup>28,31</sup>. Participants completed 7 (1 participant), 8 (2 participants) or 9 (5  
223 participants) runs.

## 224 *MRI and fMRI acquisition*

225 High resolution anatomical and functional data were acquired using a Philips Achieva 7 T scanner with  
226 a maximum gradient strength of 40 mT/m and a slew rate of 200 T/m/s (Philips, Best, The  
227 Netherlands). A dual-channel volume transmit head coil was used for all scans (Nova Medical, MA,  
228 USA). A 32-channel receive coil (Nova Medical, MA, USA) was used for all anatomical scans, and two  
229 custom-built 16-channel high-density surface receive arrays were used for all functional scans<sup>57</sup>  
230 (MRCoils BV). Positioning of these receive arrays was preformed outside the scanner. First,  
231 participants put on a cloth cap to prevent sliding of the surface arrays on their hair and facilitate  
232 accurate targeting of the region of interest. Next, the receive arrays were placed on the head, with  
233 their centers at approximately the height of electrode location CPz (following the extended 10-20  
234 system for electrode positioning), aligned with the midline of the head of the participant. The receive  
235 arrays touched each other but did not overlap. The exact positioning was varied per participant, as  
236 the process was ultimately guided by the personalized location of the most prominent topographic  
237 numerosity map in parietal cortex (NPC1), based on previous numerosity fMRI studies for all but one  
238 participant. After positioning, the receive arrays were fixed in place using PowerFlex self-adherent  
239 tape. The participant was then carefully transferred to the scanner environment. The participant was  
240 positioned such that the middle of the receive arrays (in the volume transmit coil) was approximately  
241 in the isocenter.

242 T1-weighted anatomical data for four participants were acquired using an MP2RAGE sequence<sup>58</sup>.  
243 Sequence parameters were: T11 = 800 ms, T12 = 2700 ms, TR<sub>MP2RAGE</sub> = 5500 ms, TR/TE = 6.2/2.3 ms, flip  
244 angle  $\alpha_1 = 7$ , and  $\alpha_2 = 5$ , bandwidth = 403.7 Hz/pixel, acceleration factor using SENSE encoding = 3.5 x  
245 1.3 (RL and AP respectively), resolution = 0.65 mm isotropic, whole-brain coverage, total scan time 9  
246 min 57 s. T1-weighted anatomical data for the other three participants was acquired using an MPRAGE  
247 sequence combined with a proton-density (PD)-weighted sequence. The PD-weighted acquisition was  
248 used to correct for image intensity inhomogeneities. Sequence parameters for the MPRAGE  
249 acquisition were: TR/TE = 7/2.8 ms, flip angle  $\alpha = 8$  degrees, resolution = 0.8 mm isotropic, whole-  
250 brain coverage, total scan time 4 min 56 s. Sequence parameters for the PD acquisition were: TR/TE =  
251 5.8/2.8 ms, flip angle  $\alpha = 1$  degree, resolution = 0.8 mm isotropic, whole-brain coverage, total scan  
252 time 1 min 16 s. The field of view, orientation, and location of the PD scan was identical to the  
253 MPRAGE. T1-weighted anatomical data for one participant were acquired on a 3T MRI scanner.  
254 Sequence parameters were: TR/TE = 10/4.6 ms, flip angle  $\alpha = 8$  degrees, resolution = 0.80 x 0.75 x 0.75  
255 mm, whole-brain coverage.

256 Functional data were acquired using a T2\*-weighted 3-dimensional multi-shot EPI (3D- EPI, two shots  
257 per slice, 24 slices, 48 shots overall). The sequence parameters were: TR/TE = 60/28.9 ms, flip angle:  
258 20°, acceleration factor using SENSE encoding: 3.5 (right-left) x 1.3 (anterior-posterior), echo planar  
259 factor: 37, voxel size = 0.93 mm isotropic, FOV = 119 (right-left) x 119 (feet-head) x 22.32 (anterior-  
260 posterior) mm, 24 coronal slices, and 10% oversampling in the slice direction. The volume repetition  
261 time was 1200 ms. Each functional run was 274 time frames in duration. The acquisition volume was  
262 rotated approximately 40° in the sagittal plane to assure maximum coverage of the region of interest  
263 (Figure 1B). The exact angulation differed between participants, depending on their orientation in the  
264 scanner and location of the region of interest.

265 For each functional run, we acquired an additional five volumes with reversed right-left phase-  
266 encoding. Reversing the phase-encoding direction ensured that these so-called 'topup' runs had the  
267 opposite geometrical distortions to the original volumes<sup>59</sup>.

268 *Pre-processing: anatomical data*

269 Gray/white matter classifications of the MP2RAGE anatomical data (four participants) were carried  
270 out using MIPAV (<http://mipav.cit.nih.gov/>) with the CBS-tools plugin<sup>60</sup> ([www.nitrc.org/projects/cbs-](http://www.nitrc.org/projects/cbs-tools/)  
271 [tools/](http://www.nitrc.org/projects/cbs-tools/)). For the MPRAGE anatomical data (four participants), gray/white matter classification was  
272 performed using Freesurfer (<http://surfer.nmr.mgh.harvard.edu/>). All classifications were manually  
273 optimized. After registration to the functional data (see below), these classifications were used to  
274 compute volume-preserving distance maps between the gray-white matter (GM/WM) border and the  
275 gray matter-cerebrospinal fluid (GM/CSF)<sup>61</sup>. These were computed using the Nighres processing  
276 tools<sup>40</sup>.

277 *Pre-processing: functional data*

278 Data processing was performed using AFNI<sup>62</sup> and MATLAB (Mathworks; 2015b). First, a warp field to  
279 correct for susceptibility distortions was calculated using a nonlinear transformation, with the first five  
280 de-obliqued volumes of each of the functional and topup runs as input. Subsequently, motion  
281 parameters within and between runs were estimated by aligning the volumes of each run to the first  
282 volume of the respective run (within run motion), and aligning the first volume of each run to the first  
283 volume of the first run (between run motion) using Fourier interpolation, and regressed out. Next, the  
284 first 10 volumes of each run were removed to ensure that the signal had reached a steady state. All  
285 runs were despiked using the AFNI function 3dDespike. This step was implemented to remove  
286 spurious large fluctuations in signal amplitude between two time points. These spikes were replaced  
287 with the average of the closest two non-spike time points. Then, each run was divided into four equal  
288 parts of 66 volumes each, corresponding with the four stimulus cycles. These parts were then scaled,  
289 converting the time-series information to percentage signal change by dividing the signal of each voxel  
290 by its temporal mean, multiplying that signal with 100, and subsequently subtracting 100 to ensure  
291 that the temporal mean of that voxel was zero percent signal change. First-degree polynomial  
292 detrending was then performed on all scaled partial runs to remove linear in- or decreases in the  
293 signal, using the AFNI function 3dDetrend. All detrended, scaled partial runs were then averaged and  
294 the between partial-run average temporal mean of each voxel was added to create the mean time-  
295 series. This time-series volume was then used as input for the numerosity modelling (see below under  
296 'Numerosity modelling'). The mean time-series and resulting model estimate volumes were  
297 subsequently de-obliqued, and the previously computed warp field to correct for susceptibility  
298 distortions was applied.

299 Next, the mean EPI image was computed by taking the temporal mean of the mean time-series  
300 volume. This EPI mean image was initially registered to the anatomy using a multi-step procedure. The  
301 resulting transformation matrices from this procedure were combined and subsequently applied to  
302 the anatomical data to avoid resampling of the functional data. First, the anatomy was restricted to  
303 roughly the parietal lobe using the AFNI function @clip\_volume. Next the EPI mean image was de-  
304 obliqued using the AFNI function 3dWarp. Then, the de-obliqued EPI mean image and anatomy were  
305 brought into the same space by aligning the center of mass of the anatomy to the de-obliqued EPI  
306 mean image. Then, the 'Nudge dataset' AFNI plugin was used to manually shift and rotate the de-  
307 obliqued EPI mean image to provide a good starting point for two automated registration steps. These  
308 registration steps consisted of affine transformations to further optimize the registration, using local  
309 Pearson correlation as cost function<sup>63</sup>. The first transformation allowed for a maximum rotation  
310 and/or shift of 3 mm in any direction, while the second transformation allowed for a maximum  
311 rotation and/or shift of 1 mm. These affine transformations were then applied to the manually moved,  
312 mean de-obliqued EPI image. The transformation matrices of the manual step and the two affine  
313 transformations were combined into a single affine matrix. This matrix was then inverted and applied

314 to the restricted anatomy to register it to the de-obliqued EPI mean image. The registered anatomy  
315 was then resampled to the 0.93 mm isotropic resolution and grid of the EPI mean image, and  
316 subsequently inspected visually for registration quality. The same procedure was then applied to the  
317 gray-white matter classifications.

318 Lastly, using the anatomy volume-preserving distance map volumes (see 'Pre-processing: anatomical  
319 data'), the warped model estimate volumes (cross-validated explained variance, tuning width, and  
320 preferred numerosity) were sampled across 9 cortical depths using the laminar profile sampling  
321 function in Nighres, resulting in computational 'columns' (see 'Cortical depth analysis' below for  
322 further details).

## 323 QUANTIFICATION AND STATISTICAL ANALYSIS

### 324 *Numerosity modelling*

325 Numerosity tuning for each voxel was estimated from the mean time-series data and the stimulus  
326 time course, using methods very similar to population receptive field (pRF) mapping<sup>1</sup>. These methods  
327 have previously been described by Harvey and colleagues<sup>28</sup>. This analysis was performed using  
328 MATLAB, the Vistasoft software package (<http://white.stanford.edu/software/>) and custom  
329 numerosity-modelling code from Harvey and colleagues<sup>28,31</sup>.

330 In short, we estimated the aggregate numerosity tuning of the hemodynamic consequences of the  
331 activity of neuronal populations in each voxel. This numerosity tuning consisted of a preferred  
332 numerosity, and a tuning width for each (numerosity-selective) voxel. A forward model was used to  
333 predict the aggregate population response based on the overlap of the presented numerosity at each  
334 time point in time and the numerosity tuning. This model estimated preferred numerosity and tuning  
335 width in logarithmic space as the mean and standard deviation of a Gaussian, respectively. Next, the  
336 predicted population response was convolved with a canonical two-gamma hemodynamic response  
337 function (HRF<sup>64</sup>) to make a predicted fMRI time-series. This process was repeated to create a set of  
338 predicted fMRI time-series for all combinations of a large range of preferred numerosity (67 equal  
339 steps between 0 and 2 (corresponding to 1-7.4 in linear space)) and tuning width (400 equal steps  
340 between 0.03 and 3) parameters. Note that this results in a maximum tuning width of 148 for the  
341 largest preferred numerosities. The predicted time-series were then compared to the fMRI time-series  
342 of each voxel, and the best fitting parameters for each voxel were chosen by minimizing the sum of  
343 squared errors between the predicted and measured time-series (Figure 1C, D). The best-fitting  
344 preferred numerosity and tuning width were then converted to linear space, resulting in an  
345 asymmetric Gaussian with a peak at the preferred numerosity and an tuning width estimate  
346 represented by its full width at half maximum (FWHM<sup>28</sup>, inset Figure 1E). These procedures were  
347 performed for all voxels within the field of view of the functional scans for each participant, including  
348 the white matter. This resulted in preferred numerosity and tuning width estimates, along with the  
349 explained variance of these estimates for each voxel. Next, the fitting procedure was repeated using  
350 only the odd and even runs. The parameter estimates from the odd runs and the timeseries data of  
351 the even runs and vice versa were then used to estimate the cross-validated model explained variance.  
352 The two cross-validated explained variance values for each voxel were then averaged. All reported  
353 explained variance/R<sup>2</sup> values are cross-validated.

### 354 *Cortical depth analysis*

355 Nine levelsets<sup>40</sup> were generated from white matter to the gray matter surface. A cortical depth profile  
356 was generated by iteratively growing the normal vectors from the middle levelset to intersect the  
357 closest levelset towards the gray matter surface, and storing the corresponding coordinates. The same

358 procedure was adopted to grow the profile towards white matter from the middle levelset. The two  
359 sets of coordinates were merged to form the coordinate set of a single cortical depth profile. The value  
360 assigned to each point along the profile was obtained by linear interpolation (e.g.: the profiles storing  
361 variance explained information were obtained via linear interpolation of the variance explained  
362 volume along each profile's cortical depth coordinates). One profile was assigned to each voxel within  
363 gray matter, based on the nearest obtained profile coordinate. The previous calculations were  
364 performed using Nighres. All subsequent calculations were performed using MATLAB, unless stated  
365 otherwise. Profiles from neighboring voxels sample from similar cortical locations, thus are very  
366 similar and provide redundant information. To mitigate these redundancies, we selected profiles from  
367 voxels at a given cortical depth (between 0.15 and 0.25) for further analysis. Changing the selection  
368 criteria to a different range across cortical depth did not significantly change the results (for results  
369 using a cortical depth between 0.75 and 0.85, see Figure S1C, F). Next, only those profiles for which  
370 the cross-validated model explained variance at each of the nine depths was equal to or higher than  
371 the 99<sup>th</sup> percentile cross-validated  $R^2$  in the white matter voxels included in the field of view of the  
372 functional scans for each participant, were included in the subsequent processing steps. The average  
373 number of selected profiles was  $M = 217$  ( $SD = 117$ , range = 90 - 392), while the average individual  
374 cross-validated  $R^2$  threshold was  $M = 8\%$  ( $SD = 2$  range = 5-12%). Next, we estimated a bootstrapped  
375 median fit on the preferred numerosity and tuning width for each cortical depth bin using R. These  
376 median fits were subsequently sampled at numerosity 2 and 3 to obtain the fitted tuning width. These  
377 numerosities were chosen as they were the most frequently present values on average (Figure S2B).  
378 These samples were Z-transformed for each sampled numerosity and participant separately, resulting  
379 in Z-transformed median tuning width profiles across cortical depth for each participant for  
380 numerosity 2 and 3. Next, a quadratic fit was performed for each profile, and the predictor estimates  
381 (intercept, slope, and quadratic component) of all participants were tested against zero using a one-  
382 sample t-test. For a direct comparison, we repeated this procedure, using only a linear fit (intercept  
383 and slope). For visualization purposes, a quadratic fit was performed on the aggregate Z-transformed  
384 data of all participants together, separately for each numerosity of interest (Figure 3A, C). A reverse  
385 Z-transform was then performed for this fit (Figure 3B, D).

386 As mentioned at the beginning of the results sections, due to the cortical folding of the cerebral cortex,  
387 the center of a voxel on the regular grid (isotropic acquisition, 0.93mm) could be located close to the  
388 cerebro-spinal fluid surface, close to the white matter surface or anywhere between the two, thus  
389 allowing a denser sampling rate along cortical depth. This comes at the cost of partial volume effects  
390 that can especially influence voxels located at the edge of the grey matter (close to the cerebro-spinal  
391 fluid surface, close to the white matter surface), we acknowledge this limitation. We mitigate this  
392 limitation by re-analysing our data, excluding the outermost depth bins (close to cerebrospinal fluid  
393 surface) to reduce the potential partial volume effects. These results can be found in Figure S1B and  
394 D, confirming our main findings, showing that these are unlikely to be the result of partial volume  
395 effects.

## 396 KEY RESOURCES TABLE

REAGENT or RESOURCE	SOURCE	IDENTIFIER
Deposited data		
Raw and analyzed data	This paper	
Software and algorithms		
MATLAB (Mathworks, 2015b)	<a href="http://www.mathworks.com/products/matlab/">http://www.mathworks.com/products/matlab/</a>	RRID:SCR_001622

R/rstudio (3.4.4)	<a href="http://www.r-project.org/">http://www.r-project.org/</a>	RRID:SCR_001905
Python (3.7.4/2.7.18 for AFNI)	<a href="http://www.python.org/">http://www.python.org/</a>	RRID:SCR_008394
AFNI	<a href="http://afni.nimh.nih.gov/afni/">http://afni.nimh.nih.gov/afni/</a>	RRID:SCR_005927
Nighres package for Python	<a href="https://nighres.readthedocs.io/en/latest/">https://nighres.readthedocs.io/en/latest/</a>	<a href="https://doi.org/10.1093/gigascience/giy082">https://doi.org/10.1093/gigascience/giy082</a>
Analysis code	This paper; Open Science Framework	
MIPAV	<a href="http://mipav.cit.nih.gov/">http://mipav.cit.nih.gov/</a>	RRID:SCR_007371
Freesurfer	<a href="http://surfer.nmr.mgh.harvard.edu/">http://surfer.nmr.mgh.harvard.edu/</a>	RRID:SCR_001847
Vistasoft	<a href="http://white.stanford.edu/software/">http://white.stanford.edu/software/</a>	

## 397 Acknowledgements

398 This work has supported by the European Union's Horizon 2020 research and innovation program  
399 under the Marie Skłodowska- Curie grant agreement No 641805 (SOD), Ammodo KNAW Award (SOD),  
400 and Netherlands Organization for Scientific Research (NWO) Vici grant 016.Vici.185.050 (SOD) and Vidi  
401 grant 13339 (NP). AF is supported by a grant from the Biotechnology and Biology research council  
402 (BBSRC, grant number: BB/S006605/1) and the Bial Foundation, Bial Foundation Grants Programme  
403 2020/21, A-29315;. NP is supported by a grant from the National Institutes of Mental Health of the  
404 National Institutes of Health (R01MH111417). The Spinoza Centre is a joint initiative of the Amsterdam  
405 University Medical Center, VU University, Netherlands Institute for Neuroscience, and the Royal  
406 Netherlands Academy of Sciences.

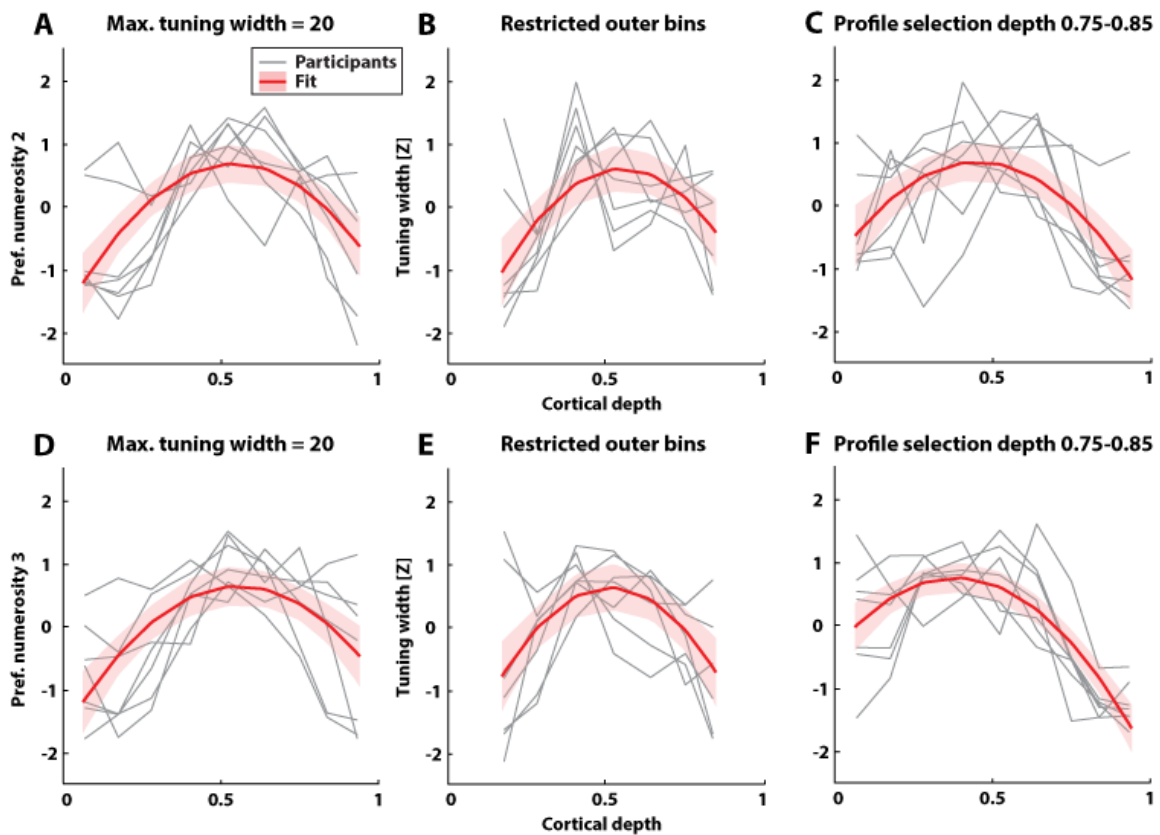
## 407 Author contributions

408 JAvD and SOD designed the experiment; JAvD collected the data; JAvD and AF analyzed the data; all  
409 authors contributed to and reviewed the manuscript text; JAvD prepared all figures; SOD, NP, and AF  
410 provided general supervision and guidance throughout.

## 411 Declaration of Interests

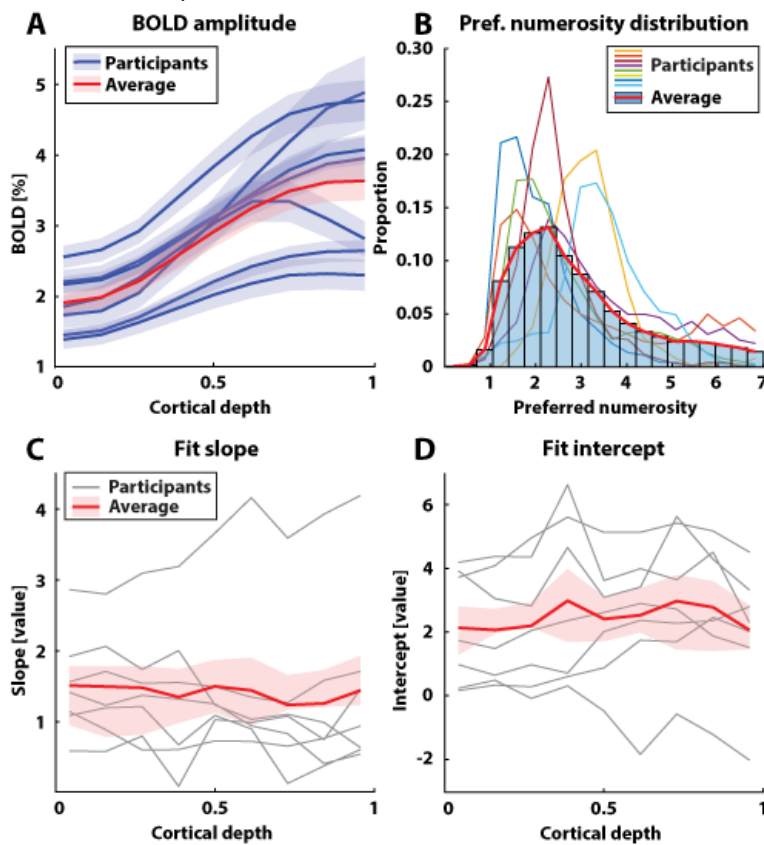
412 The authors declare no competing interests.

413 Supplementary material  
 414 Alternative analysis parameters



415  
 416 *Figure S1: Changing analysis parameters does not significantly change the main findings. Same*  
 417 *analysis as in the main manuscript, but with: a maximum tuning width of 20 (A, D); the outer depth*  
 418 *bins removed to control for partial volume effects (B, E); and a different profile depth selection*  
 419 *criterion (cortical depth between 0.75 and 0.85, rather than the 0.15-0.25 in the main manuscript, C, F). A-C) Z-*  
 420 *scored tuning width, sampled at preferred numerosity 2 from the median fits for each depth bin. Fit*  
 421 *parameter values were: A) slope = 9.01, quadratic component = -8.30;  $t(6)_{slope} = 6.57, p < 0.001,$*   
 422  *$t(6)_{quadratic} = -8.65, p < 0.001.$  B) slope = 12.55, quadratic component = -11.43;  $t(6)_{slope} = 4.30, p < 0.01,$*   
 423  *$t(6)_{quadratic} = -5.06, p < 0.01.$  C) slope = 6.97, quadratic component = -7.72;  $t(6)_{slope} = 4.00, p < 0.01,$*   
 424  *$t(6)_{quadratic} = -4.40, p < 0.01.$  D-F) Same as A-C, but sampled at preferred numerosity 3. Fit parameter*  
 425 *values were: D) slope = 8.44, quadratic component = -7.56;  $t(6)_{slope} = 7.39, p < 0.001, t(6)_{quadratic} = -5.92,$*   
 426  *$p < 0.001.$  E) slope = 12.16, quadratic component = -11.85;  $t(6)_{slope} = 3.28, p < 0.05, t(6)_{quadratic} = -3.93,$*   
 427  *$p < 0.01.$  F) slope = 5.91, quadratic component = 7.70;  $t(6)_{slope} = 3.24, p < 0.05, t(6)_{quadratic} = -5.52, p <$*   
 428 *0.01. A-F) Gray lines represent individual participants. Red lines represent the best second-degree*  
 429 *polynomial fit. Shaded regions represent the 95% between-participant confidence interval of the fit.*

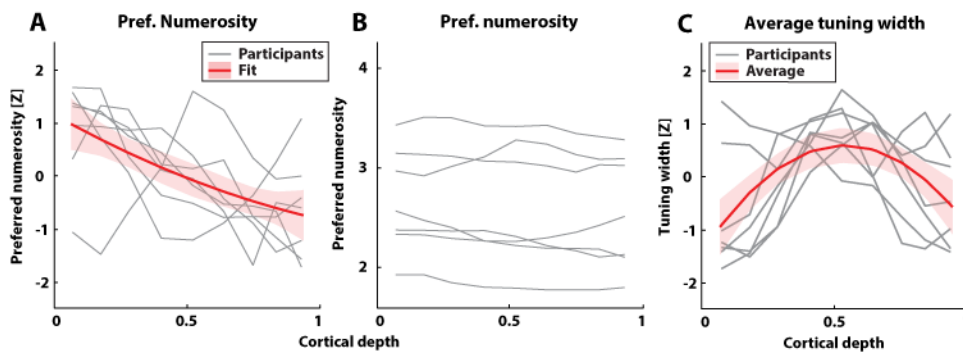
430 Control analyses



431

432 *Figure S2: Control analyses: A) BOLD amplitude increases towards the cortical surface for most*  
 433 *participants. Blue lines represent individual participants. Red lines represent group averages. Shaded*  
 434 *regions denote the standard error of the mean. B) Proportion of profiles per preferred numerosity.*  
 435 *Colored lines represent distributions of individual participants. Blue histogram and red line represent*  
 436 *the group-average distribution. C,D) Median fit slope (C) and intercept (D) across cortical depth for*  
 437 *individual participants. Analysis parameters from the main analysis. Gray lines represent individual*  
 438 *participants. Red lines represent group averages. Shaded regions represent the standard error of the*  
 439 *mean. Note that while the fit and intercept values do not directly show the pattern found in the main*  
 440 *manuscript, the Z-transformed linear combination of the two does.*

441 Average preferred numerosity does not vary across cortical depth, while average tuning  
 442 width does

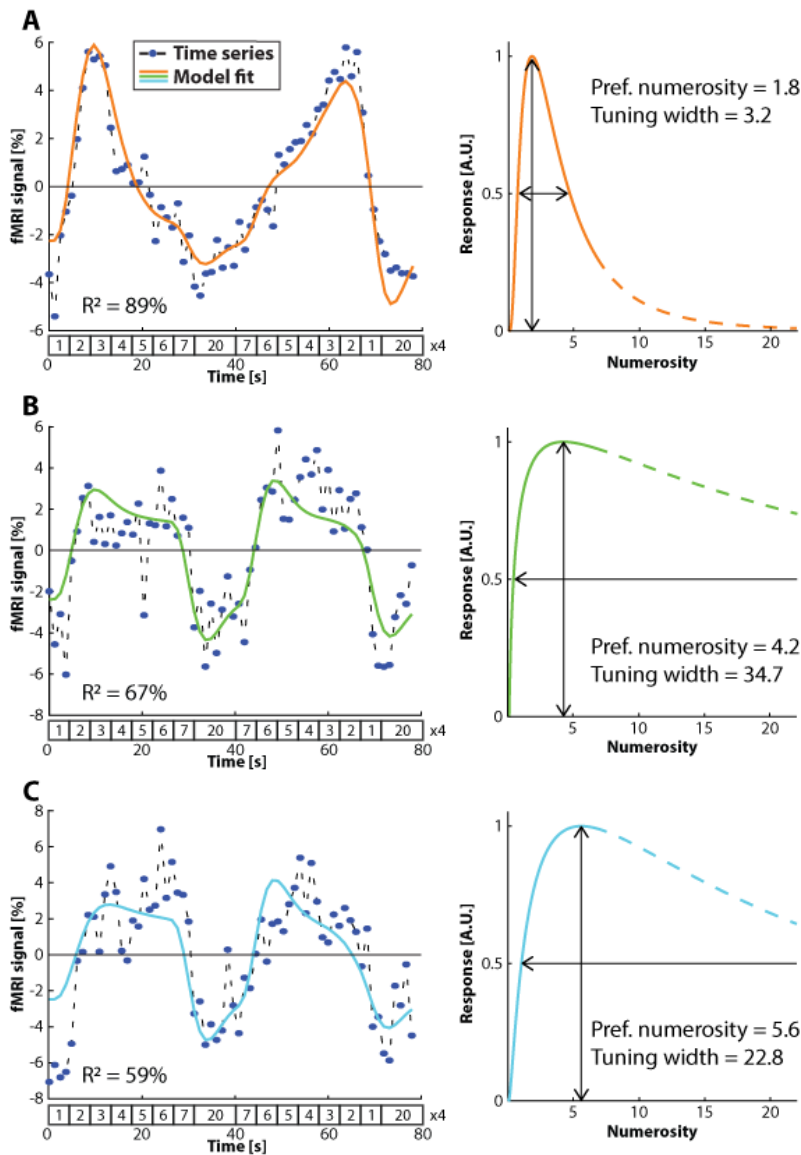


443

444 *Figure S3: Average preferred numerosity across cortical depth. A) Z-scored preferred numerosity across*  
 445 *cortical depth. Slope and quadratic component of the fit were non-significant. Shaded region*  
 446 *represents the 95% between-participant confidence interval of the fit. B) Preferred numerosity across*  
 447 *cortical depth for all participants. C) Z-scored median tuning width across cortical depth (no sampling*

448 at a specific numerosity). Fit: slope = 7.43, quadratic component = -6.96;  $t(6)_{slope} = 4.65$ ,  $p < 0.01$ ,  
 449  $t(6)_{quadratic} = -4.5$ ,  $p < 0.01$ .

450 Example time-series and model fits



451  
 452 Figure S4: Time-series of example voxels (left column, dashed lines with blue discrete timepoints)  
 453 overlaid with best fitting predicted fMRI response (solid lines) and associated tuning model (right  
 454 column). Dashed parts of the tuning model represent estimated responses to numerosities not  
 455 included in the stimulus range (except for numerosity 20).

456 References

457 1. Dumoulin, S. O. & Wandell, B. A. Population receptive field estimates in human visual cortex.  
 458 *Neuroimage* **39**, 647–660 (2008).  
 459 2. Harvey, B. M. & Dumoulin, S. O. The Relationship between Cortical Magnification Factor and  
 460 Population Receptive Field Size in Human Visual Cortex: Constancies in Cortical Architecture.  
 461 *J. Neurosci.* **31**, 13604–13612 (2011).  
 462 3. Hubel, D. H. & Wiesel, T. N. Uniformity of monkey striate cortex: A parallel relationship  
 463 between field size, scatter, and magnification factor. *J. Comp. Neurol.* **158**, 295–305 (1974).

- 464 4. Quiroga, R. Q., Reddy, L., Kreiman, G., Koch, C. & Fried, I. Invariant visual representation by  
465 single neurons in the human brain. *Nature* **435**, 1102–1107 (2005).
- 466 5. Anderson, J. C. & Martin, K. A. C. The synaptic connections between cortical areas V1 and V2  
467 in macaque monkey. *J. Neurosci.* **29**, 11283–11293 (2009).
- 468 6. Felleman, D. J. & Van Essen, D. C. Distributed hierarchical processing in the primate cerebral  
469 cortex. *Cereb. Cortex* **1**, 1–47 (1991).
- 470 7. Markov, N. T. & Kennedy, H. The importance of being hierarchical. *Current Opinion in*  
471 *Neurobiology* vol. 23 187–194 (2013).
- 472 8. Rockland, K. S. & Pandya, D. N. Laminar origins and terminations of cortical connections of  
473 the occipital lobe in the rhesus monkey. *Brain Res.* **179**, 3–20 (1979).
- 474 9. Wong-Riley, M. Columnar cortico-cortical interconnections within the visual system of the  
475 squirrel and macaque monkeys. *Brain Res.* **162**, 201–217 (1979).
- 476 10. Graham, J., Lin, C. -S & Kaas, J. H. Subcortical projections of six visual cortical areas in the owl  
477 monkey, *Aotus trivirgatus*. *J. Comp. Neurol.* **187**, 557–580 (1979).
- 478 11. Dumoulin, S. O., Fracasso, A., van der Zwaag, W., Siero, J. C. W. & Petridou, N. Ultra-high field  
479 MRI: Advancing systems neuroscience towards mesoscopic human brain function.  
480 *Neuroimage* **168**, 345–357 (2018).
- 481 12. De Martino, F. *et al.* The impact of ultra-high field MRI on cognitive and computational  
482 neuroimaging. *Neuroimage* **168**, 366–382 (2018).
- 483 13. Lawrence, S. J. D., Formisano, E., Muckli, L. & de Lange, F. P. Laminar fMRI: Applications for  
484 cognitive neuroscience. *NeuroImage* (2017) doi:10.1016/j.neuroimage.2017.07.004.
- 485 14. Stephan, K. E. *et al.* Laminar fMRI and computational theories of brain function. *NeuroImage*  
486 vol. 197 699–706 (2019).
- 487 15. Fracasso, A., Petridou, N. & Dumoulin, S. O. Systematic variation of population receptive field  
488 properties across cortical depth in human visual cortex. *Neuroimage* **139**, 427–438 (2016).
- 489 16. Hubel, D. H. & Wiesel, T. N. Receptive fields and functional architecture of monkey striate  
490 cortex. *J. Physiol.* **195**, 215–243 (1968).
- 491 17. Self, M. W., van Kerkoerle, T., Goebel, R. & Roelfsema, P. R. Benchmarking laminar fMRI:  
492 Neuronal spiking and synaptic activity during top-down and bottom-up processing in the  
493 different layers of cortex. *NeuroImage* vol. 197 806–817 (2019).
- 494 18. Ninomiya, T., Dougherty, K., Godlove, D. C., Schall, J. D. & Maier, A. Microcircuitry of  
495 agranular frontal cortex: Contrasting laminar connectivity between occipital and frontal  
496 areas. *J. Neurophysiol.* **113**, 3242–3255 (2015).
- 497 19. Callaway, E. M. Local Circuits in Primary Visual Cortex of the Macaque Monkey. *Annu. Rev.*  
498 *Neurosci.* **21**, 47–74 (1998).
- 499 20. Douglas, R. J. & Martin, K. A. C. Neuronal circuits of the neocortex. *Annu. Rev. Neurosci.* **27**,  
500 419–451 (2004).
- 501 21. Gilbert, C. D. Microcircuitry of the Visual Cortex. *Annu. Rev. Neurosci.* **6**, 217–247 (1983).
- 502 22. Piazza, M. Neurocognitive Start-Up Tools for Symbolic Number Representations. in *Space,*  
503 *Time and Number in the Brain* 267–285 (Elsevier Inc., 2011). doi:10.1016/B978-0-12-385948-  
504 8.00017-7.

- 505 23. Halberda, J., Mazocco, M. M. M. & Feigenson, L. Individual differences in non-verbal number  
506 acuity correlate with maths achievement. *Nature* **455**, 665–668 (2008).
- 507 24. Harvey, B. M. Quantity cognition: Numbers, numerosity, zero and mathematics. *Current*  
508 *Biology* vol. 26 R419–R421 (2016).
- 509 25. Dehaene, S. *The number sense : how the mind creates mathematics*. (Oxford University Press,  
510 1997).
- 511 26. Nieder, A. & Miller, E. K. Coding of cognitive magnitude: Compressed scaling of numerical  
512 information in the primate prefrontal cortex. *Neuron* **37**, 149–157 (2003).
- 513 27. Knops, A., Piazza, M., Sengupta, R., Eger, E. & Melcher, D. A shared, flexible neural map  
514 architecture reflects capacity limits in both visual short-term memory and enumeration. *J.*  
515 *Neurosci.* **34**, 9857–9866 (2014).
- 516 28. Harvey, B. M., Klein, B. P., Petridou, N. & Dumoulin, S. O. Topographic Representation of  
517 Numerosity in the Human Parietal Cortex. *Science (80-. )*. **341**, 1123–1126 (2013).
- 518 29. Piazza, M., Izard, V., Pinel, P., Le Bihan, D. & Dehaene, S. Tuning curves for approximate  
519 numerosity in the human intraparietal sulcus. *Neuron* **44**, 547–555 (2004).
- 520 30. Nieder, A., Freedman, D. J. & Miller, E. K. Representation of the quantity of visual items in the  
521 primate prefrontal cortex. *Science (80-. )*. **297**, 1708–1711 (2002).
- 522 31. Harvey, B. M. & Dumoulin, S. O. A network of topographic numerosity maps in human  
523 association cortex. *Nat. Hum. Behav.* **1**, 0036 (2017).
- 524 32. Petridou, N. & Siero, J. C. W. Laminar fMRI: What can the time domain tell us? *Neuroimage*  
525 (2017) doi:10.1016/j.neuroimage.2017.07.040.
- 526 33. Self, M. W. & Roelfsema, P. R. Paying Attention to the Cortical Layers. *Neuron* **93**, 9–11  
527 (2017).
- 528 34. Cantlon, J. F. *et al.* The neural development of an abstract concept of number. *J. Cogn.*  
529 *Neurosci.* **21**, 2217–2229 (2009).
- 530 35. Dehaene, S., Spelke, E., Pinel, P., Stanescu, R. & Tsivkin, S. Sources of mathematical thinking:  
531 Behavioral and brain-imaging evidence. *Science (80-. )*. **284**, 970–974 (1999).
- 532 36. Eger, E. *et al.* Deciphering Cortical Number Coding from Human Brain Activity Patterns. *Curr.*  
533 *Biol.* **19**, 1608–1615 (2009).
- 534 37. Pinel, P. *et al.* Event-related fMRI analysis of the cerebral circuit for number comparison.  
535 *Neuroreport* **10**, 1473–1479 (1999).
- 536 38. Hofstetter, S., Cai, Y., Harvey, B. M. & Dumoulin, S. O. Topographic maps representing haptic  
537 numerosity reveals distinct sensory representations in supramodal networks. *Nat. Commun.*  
538 **12**, 1–13 (2021).
- 539 39. Cai, Y. *et al.* Topographic numerosity maps cover subitizing and estimation ranges. *Nat.*  
540 *Commun.* **12**, 3374 (2021).
- 541 40. Huntenburg, J. M., Steele, C. J. & Bazin, P. L. Nighres: processing tools for high-resolution  
542 neuroimaging. *Gigascience* **7**, 1–9 (2018).
- 543 41. Fischl, B. & Dale, A. M. Measuring the thickness of the human cerebral cortex. *Neuroimage* **9**,  
544 (1999).

- 545 42. Callaway, E. M. Local circuits in primary visual cortex of the macaque monkey. *Annu. Rev. Neurosci.* **21**, 47–74 (1998).  
546
- 547 43. Duvernoy, H. M., Delon, S. & Vannson, J. L. Cortical blood vessels of the human brain. *Brain Res. Bull.* **7**, 519–579 (1981).  
548
- 549 44. Siero, J. C. W., Petridou, N., Hoogduin, H., Luijten, P. R. & Ramsey, N. F. Cortical depth-dependent temporal dynamics of the BOLD response in the human brain. *J. Cereb. Blood Flow Metab.* **31**, 1999–2008 (2011).  
550  
551
- 552 45. van Dijk, J. A., Fracasso, A., Petridou, N. & Dumoulin, S. O. Linear systems analysis for laminar fMRI: Evaluating BOLD amplitude scaling for luminance contrast manipulations. *Sci. Rep.* **10**, 5462 (2020).  
553  
554
- 555 46. Weber, B., Keller, A. L., Reichold, J. & Logothetis, N. K. The microvascular system of the striate and extrastriate visual cortex of the macaque. *Cereb. Cortex* **18**, 2318–2330 (2008).  
556
- 557 47. Polimeni, J. R., Fischl, B., Greve, D. N. & Wald, L. L. Laminar analysis of 7T BOLD using an imposed spatial activation pattern in human V1. *Neuroimage* **52**, 1334–1346 (2010).  
558
- 559 48. Kim, J. H. & Ress, D. Reliability of the depth-dependent high-resolution BOLD hemodynamic response in human visual cortex and vicinity. *Magn. Reson. Imaging* **39**, 53–63 (2017).  
560
- 561 49. Muckli, L. *et al.* Contextual Feedback to Superficial Layers of V1. *Curr. Biol.* **25**, 2690–2695 (2015).  
562
- 563 50. Biswal, B., DeYoe, E. A. & Hyde, J. S. Reduction of physiological fluctuations in fMRI using digital filters. *Magn. Reson. Med.* **35**, 107–113 (1996).  
564
- 565 51. Wowk, B., McIntyre, M. C. & Saunders, J. K. k-Space detection and correction of physiological artifacts in fMRI. *Magn. Reson. Med.* **38**, 1029–1034 (1997).  
566
- 567 52. Krüger, G. & Glover, G. H. Physiological noise in oxygenation-sensitive magnetic resonance imaging. *Magn. Reson. Med.* **46**, 631–637 (2001).  
568
- 569 53. Cambridge Research Systems. BOLDscreen 32 LCD for fMRI. <http://www.crsLtd.com/tools-for-functional-imaging/mr-safe-displays/boldscreen-32-lcd-for-fmri/nest/boldscreen-32-technical-specification#npm> (2012).  
570  
571
- 572 54. Brainard, D. H. The Psychophysics Toolbox. *Spat. Vis.* **10**, 433–436 (1997).
- 573 55. Pelli, D. G. the Videotoolbox Software for Visual Psychophysics: Transforming Numbers Into Movies. *Spat. Vis.* **10**, 437–442 (1997).  
574
- 575 56. Harvey, B. M. *et al.* Frequency specific spatial interactions in human electrocorticography: V1 alpha oscillations reflect surround suppression. *Neuroimage* **65**, 424–432 (2013).  
576
- 577 57. Petridou, N. *et al.* Pushing the limits of high-resolution functional MRI using a simple high-density multi-element coil design. *NMR Biomed.* **26**, 65–73 (2013).  
578
- 579 58. Marques, J. P. *et al.* MP2RAGE, a self bias-field corrected sequence for improved segmentation and T1-mapping at high field. *Neuroimage* **49**, 1271–1281 (2010).  
580
- 581 59. Andersson, J. L. R., Skare, S. & Ashburner, J. How to correct susceptibility distortions in spin-echo echo-planar images: Application to diffusion tensor imaging. *Neuroimage* **20**, 870–888 (2003).  
582  
583
- 584 60. Bazin, P. L. *et al.* Volumetric neuroimage analysis extensions for the MIPAV software package. *J. Neurosci. Methods* **165**, 111–121 (2007).  
585

- 586 61. Waehnert, M. D. *et al.* Anatomically motivated modeling of cortical laminae. *Neuroimage* **93**,  
587 210–220 (2014).
- 588 62. Cox, R. W. AFNI: Software for Analysis and Visualization of Functional Magnetic Resonance  
589 Neuroimages. *Comput. Biomed. Res.* **29**, 162–173 (1996).
- 590 63. Saad, Z. S. *et al.* Alignment using Local Pearson Correlation. *Ratio* **44**, 839–848 (2010).
- 591 64. Friston, K. J. *et al.* Event-related fMRI: Characterizing differential responses. *Neuroimage* **7**,  
592 30–40 (1998).
- 593